Andre Bergmann, Johannes Grabis, Miriana Vadala, Alexei Nefedov, Kurt Westerholt, Hartmut Zabel

Ruhr-Universität Bochum, Bochum, Germany

Heusler films and multilayers: X-ray resonant magnetic scattering and polarized neutron reflectivity studies on the relation between structure and magnetism

Dedicated to Professor Dr. Reiner Kirchheim on the occasion of his 65th birthday

We have studied the structural properties and the magnetization density profiles in multilayers of the Heusler phase Co_2MnGe with three different spacer layers: V, Au, and AlO_x, using hard X-ray scattering, soft X-ray resonant magnetic scattering, and polarized neutron reflectivity. We have found that the spacer layer has a significant effect on the magnetization profile of the Co_2MnGe layer. In all cases the interlayers at the top and the bottom of the Heusler layer exhibit a reduced magnetic moment, the thickness of which depends on the spacer layer and increases from 0.5 nm for V, to 0.6 nm for Au and 1 nm for AlO_x.

Keywords: Heusler alloys; Defects; Site disorder; X-ray resonant magnetic scattering; Polarized neutron reflection

1. Introduction

In recent years an upsurge of interest has been noticed in the new material class of ferromagnetic metals with 100 % spin polarization, so called half-metals, since they have the potential to play an important role in the rapidly evolving field of magneto-electronics (spintronics) [1–3]. The half-metallicity was first predicted 1983 by de Groot et al. for the half-Heusler alloy NiMnSb [4]. Heusler alloys are ternary intermetallic compounds with the general composition X_2YZ, X and Y being transition metal atoms and Z a non-magnetic atom. The fully ordered Heusler structure is a cubic lattice with four interpenetrating fcc sublattices occupied by X, Y and Z atoms ($L2_1$ structure). Intense theoretical investigations using energy band structure calculations predicted more than 20 different Heusler alloys to exhibit half-metallic behavior [5–9]. The most prominent are the half-metals NiMnSb and PtMnSb (so-called half-Heusler compounds, since one of the sublattices is empty), the pseudo-ternary phase $Co_2Cr_{0.6}Fe_{0.4}Al$, and the phases Co_2MnSi and Co_2MnGe. Currently the half-metallic Heusler phases are considered to be the most attractive candidates for application in spintronic devices, since they exhibit extremely high Curie temperatures (905 K for Co_2MnGe) and an electronic structure which is closely related to conventional semiconductors.

Regardless of these promising properties of the Heusler half-metals, experimental investigations in recent years have revealed that it is very difficult to realize the predicted full spin polarization even in single crystals. The performance of tunneling magneto-resistance (TMR) devices using Heusler thin films as an electrode was somewhat disappointing at first. NiMnSb integrated into a magnetic tunnel junction (MTJ) showed only 25 % spin polarization at 4.2 K [10]. Later these results were improved and actually the highest value obtained for spin polarization in an MTJ using a Co_2MnSi electrode is 89 % [11, 12]. However, irrespective of the experimental method applied to determine the degree of spin polarization quantitatively, it is always definitely less than 100 %. The main reason suggested for this reduction is site disorder in the film and at the interfaces, since only a perfectly ordered Heusler alloy exhibits a gap in the minority spin band [13, 14]. Interfaces in thin film heterostructures combining the Heusler alloys with other materials are of utmost importance for spintronic devices, since the spin polarization has to be stable down to the first few monolayers of the interface. However, these compounds are prone to interdiffusion and site disorder, which both have the tendency to suppress the full spin polarization [13, 14].

2. Structure and magnetism of bulk Heusler compounds

2.1. Structure of Heusler compounds

Discovered more than 100 years ago by Friedrich Heusler [15], the first ternary metallic compound Cu_2MnAl exhibits remarkable magnetic properties, as it is a ferromagnet even though none of its constituents is one. Further investigations showed that a whole class of isostructural ternary metallic alloys with the general composition X_2YZ exists, where X denotes a transition metal element such as Ni, Co, Fe or Pt, Y is a second transition metal element, e. g. Mn, Cr or Ti, and Z is an atom from the 3rd, 4th or 5th group of the periodic system such as Al, Ge, Sn, or Sb. More than 1000 different Heusler compounds have been synthesized
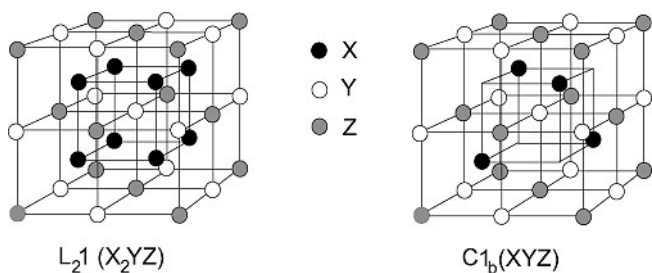
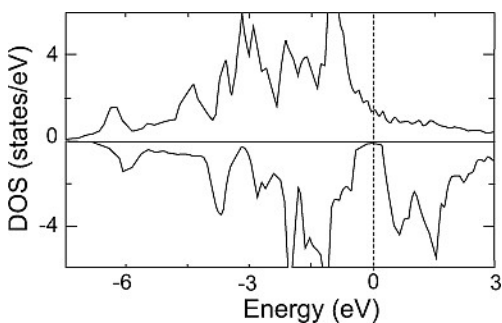Fig. 1. Schematic representation of the L2$_1$ and C1$_b$ structure.

Fig. 2. Calculated spin-projected DOS for Co$_2$MnGe, taken from Ref. [18].

so far, a comprehensive review of the experimental work up to the year 1987 can be found in Ref. [16]. They attracted considerable interest due to their very versatile magnetism. Actually, the driving force for the intense study of the Heusler compounds is the predicted half-metallic ferromagnetic nature for some of these alloys [5, 6, 17–19].

The Heusler alloys are defined as ternary intermetallic compounds with the stoichiometric composition X$_2$YX and the crystal structure L2$_1$. Moreover there exist so-called half-Heusler phases with the general formula XYZ, having C1$_b$ structure. The L2$_1$ or C1$_b$ structure is most important for the predicted half-metallic properties of the Heusler compounds, since the theoretical band structure calculations usually refer to this structure. The L2$_1$ unit cell is depicted in Fig. 1. It can be imagined to consist of four interpenetrating fcc sublattices occupied by X, X, Y and Z atoms, respectively. The sublattices are shifted along the space diagonal with the corner of the Z sublattice at (0, 0, 0), the first X sublattice at (1/4, 1/4, 1/4), the Y sublattice at (1/2, 1/2, 1/2) and the second X sublattice at (3/4, 3/4, 3/4). In the C1$_b$ structure the second X sublattice remains empty.

2.2. Magnetic properties

The majority of the Heusler alloys with a magnetic element on the Y position order ferromagnetically, but several anti-ferromagnetic compounds also exist, for instance Ni$_2$MnAl or Pd$_2$MnAl [20, 21]. The main contribution to the magnetic moments in the Heusler alloys usually stems from the atoms at the Y position. If magnetic atoms occupy the X positions, their moment is usually quite small or even vanishing. There exist a few Heusler compounds with rather large magnetic moments on both the X and the Y positions. In this case the ferromagnetic state is very stable and the ferromagnetic Curie temperature T_c becomes exceptionally high. The best examples are provided by the Heusler phases Co$_2$MnSi and Co$_2$FeSi with a Co moment

of about 1 μ_B and Curie temperatures of 985 K [22] and 1100 K [23], respectively, the highest T_c values known for the Heusler alloys. The mechanism which stabilizes the ferromagnetism is a strong next-nearest neighbor ferromagnetic exchange interaction between the spins at the X and the Y position [5, 24]. If a non-magnetic element occupies the X position, the dominant exchange interaction between the Y spins is that of a weaker superexchange type due to hybridization, mediated by the electrons of the non-magnetic Z atoms. Depending on the valence of Z the interaction can have either sign [24]. The Si sp atom has a very small negative moment which is two orders of magnitude smaller than the Co moment. The orbital moments are almost completely quenched and their magnitudes are negligible with respect to the spin magnetic moments [18, 25]. Heusler compounds such as Cu$_2$MnAl with a magnetic moment only on the Y position are considered as good examples of localized 3d metallic magnetism [24]. Since in the ideal L2$_1$ structure there are no Mn−Mn nearest neighbors, the Mn 3d wave functions overlap only weakly and the magnetic moments remain essentially localized at the Mn position.

2.3. Half metallicity

The most spectacular property of full spin polarization at the Fermi level E_F was first detected in 1983 for the half-Heusler alloy NiMnSb by electron energy band calculations [4]. PtMnSb and CoMnSb have also been predicted to possess this property. NiMnSb, PtMnSb and CoMnSb have been dubbed half-metals [4], since only for one spin direction is there metallic conductivity, for the other spin direction the conductivity is of semiconducting type. In a ferromagnetic transition metal alloy this half-metallicity is a very rare property, since usually s or p bands with a small exchange splitting cross the Fermi energy and contribute states of both spin directions. For several years the half-Heusler alloys PtMnSb, NiMnSb and CoMnSb remained the only ferromagnetic alloys with half-metallic character, before starting in 1990 a second group of half-metallic Heusler alloys, Co$_2$MnSi, Co$_2$MnGe and Co$_2$Mn(Sb$_x$Sn$_{1-x}$) were found theoretically [17, 26, 27]. The calculated indirect band gap for the minority carriers is smaller in these materials than in the half-Heusler compounds [25], for Co$_2$MnSi and Co$_2$MnGe one derives $E_{gap} = 0.81$ eV and $E_{gap} = 0.54$ eV, respectively. The spin-projected density of states for Co$_2$MnGe is depicted in Fig. 2.

The origin of the gap in the minority spin band is rather subtle, but recently theoretical calculations revealed the basic mechanism for the formation of the gap. The d–d hybridization between the transition atoms composing Heusler alloys is essential for the formation of the gap at E_F. In the case of half-Heusler compounds (e.g. NiMnSb) the gap is created by the hybridization and bonding–antibonding splitting between the Mn d and the Ni d states. In the case of full Heusler alloys (e.g. Co$_2$MnGe) the gap originates from the hybridization of the d states of the two Co atoms and the subsequent interaction of these hybrids with the Mn d states [7].

Spin polarized neutron diffraction measurements on bulk Co$_2$Mn(Si, Ge, Sn) Heusler compounds have been employed to determine the degree of spin polarization at the

Review

A. Bergmann et al. Heusler films and multilayers: X-ray resonant magnetic scattering

Fermi level [28]. This method probes the spatial distribution of the magnetization, details of which depend sensitively on the spin polarization. The results suggest a finite density of states in the minority spin d band of manganese. Hence the spin polarization was found to be large, but not 100%. More recent superconducting/ferromagnetic point contact measurements on a Co_2MnSi single crystal gave a spin polarization of 55% [29]. Similarly, the degree of spin polarization determined from the analysis of spin resolved photoemission spectra was always found to be significantly below 100% [30, 31].

2.4. Order and disorder at interfaces

Although the TMR results show that Heusler-based magnetic electrodes are quite promising, the experimentally determined spin polarization is always significantly smaller than 100%. This experience leads to the suspicion that at least for a few monolayers at the interfaces the full spin polarization is lost.

Interfaces of the Heusler compounds with other materials are a very delicate problem for spintronic devices. For spin injection into semiconductors or for TMR devices the spin polarization of the first few monolayers at the interfaces is of utmost importance. A large spin polarization in the bulk of a Heusler compound does not guarantee that it is a good
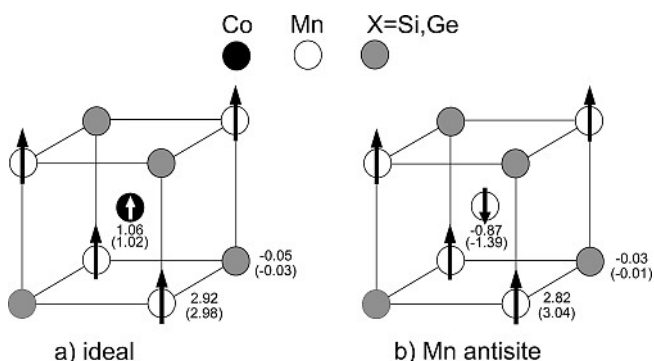

Fig. 3. Magnetic moments for (a) the ideal system and (b) the Mn antisite system in Co_2MnSi (Co_2MnGe) around the defect. Values are taken from Ref. [18].
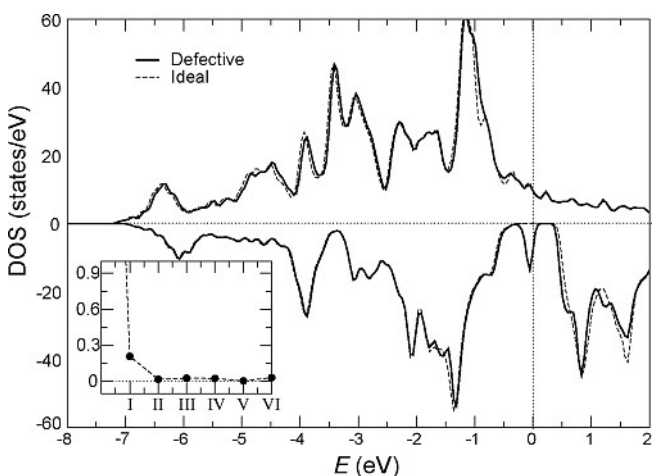

Fig. 4. Total DOS for defective (boldline) and ideal (dashed line) Co_2MnSi with Co antisite. The inset shows the minority DOS at E_F projected on the different neighbors (denoted as roman numerals) as one moves away from the Co antisite defect [18].
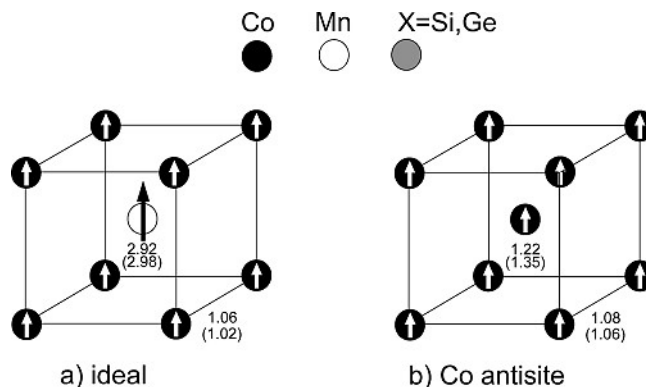
Fig. 5. Magnetic moments for (a) the ideal system and (b) the Co antisite system in Co_2MnSi (Co_2MnGe) around the defect [18].

spintronic material, unless it keeps its spin polarization down to the interfaces. Hence there are various problems that have to be overcome in order to reach full spin polarization in real devices.

Site disorder within the sublattices of the Heusler compounds disturbs the perfect $L2_1$ point symmetry and may therefore destroy the half-metallicity. An essential question is, which type of disorder is most detrimental for the spin polarization. Therefore, the effects of several types of defects in the Heusler alloys Co_2MnSi and Co_2MnGe have been studied by model calculations [6]. According to those calculations, the most frequent defects expected are: 1) Mn antisites where a Co atom is replaced by Mn, 2) Co antisites where Mn atoms are replaced by Co, and 3) Co−Mn swaps with exchanged positions compared to the ideal bulk. Due to their low formation energy, Co and Mn antisites are likely to be formed with a concentration as high as 8% [8, 32], whereas Co−Mn swaps exhibit lower defect concentrations.

Mn antisite defects are most likely to occur in Co_2Mn (Si, Ge). In this case the total density of states (DOS) shows a shift of 0.04 eV towards higher binding energies in the minority spin band, resulting in a small increase of the spin gap. For this type of antisite disorder the half-metallicity is kept. However, the Mn magnetic moment is now antiferromagnetically coupled to the surrounding Mn spins, leading to a reduction in the saturation. Figure 3 depicts the region close to the defect compared with the ideal case, including the magnetic moments. Since the point defect induced changes are efficiently screened by the conduction electrons, only the nearest neighbor spins are affected.

Although Co antisites are theoretically expected to occur in concentrations typically two orders of magnitude smaller than for Mn antisites, experimentally these two defects are found to have the same density. The Mn atom sitting on the Co position leads to a sharp peak in the electron DOS located just in proximity to the Fermi level (see Fig. 4) and therefore destroys the half-metallicity. The calculated spin polarization for the case presented in Fig. 4 is as low as 6%. The defect-induced states at the Fermi level are spatially localized, as shown in the inset of Fig. 4. The analysis of magnetic moments (Fig. 5) shows that in the case of a Co antisite defect the magnetic moments remain virtually unchanged and couple ferromagnetically to the surrounding Co spins.

Co−Mn swaps can be viewed as the sum of two different Mn and Co atomic antisites. The calculated minority DOS

R Review

A. Bergmann et al. Heusler films and multilayers: X-ray resonant magnetic scattering

is shifted to higher energies, along with a defect-induced peak located -0.2 eV below the Fermi level, the majority DOS remains essentially unaffected. Hence the half-metallic character is kept by the Co−Mn swaps. However, the total magnetic moment per unit cell is drastically reduced by about $4\,\mu_B$.

This low degree of point disorder tolerable for the Heusler compounds presents a strong experimental challenge, since in thin films a larger amount of disorder than in the bulk material is expected due to lower preparation temperatures. The best choice to avoid disorder is to grow thin films epitaxially in the well ordered $L2_1$ structure, as has been realized for Co_2MnGe on GaAs [32–34] and MgO [35]. Another possibility to avoid point defects is to find Heusler alloys with particularly high energies for the defect formation.

For high-performance spintronic devices it is of special importance to restore the half-metallic ferromagnetism at the interfaces with an isolator or semiconductor. Theoretical model calculations were first carried out for NiMnSb/ semiconductor interfaces [36, 37], mainly showing the loss of half-metallicity at the interfaces, except in the case of NiMnSb/CdS. Further calculations revealed the presence of interface states at almost all Heusler/semiconductor contacts [38, 39]. Here, the half-metallicity is destroyed only for a few atomic layers close to the interface and completely restored far away from it.

3. Experimental procedures

We have studied the structure and magnetism of the ferromagnetic Heusler compound Co_2MnGe in high-quality Co_2MnGe/Au, Co_2MnGe/V and Co_2MnGe/AlO_x multilayers with varying thicknesses of the spacer layer but with a fixed number of 50 or 30 periods. We used hard X-ray scattering, soft X-ray resonant magnetic scattering (XRMS), and polarized neutron reflectivity (PNR). The samples were prepared by rf-sputtering from solid targets with proper stoichiometry at a pressure of 5×10^{-3} mbar Ar and a substrate temperature of $300\,°C$ on $Al_2O_3(11\bar{2}0)$ substrates, as described in detail elsewhere [40]. Hard X-ray scattering was performed at the synchrotron facility HASYLAB, XRMS was carried out at the synchrotron facility BESSY II using the ALICE chamber [41], and PNR was done at the Institut Laue-Langevin using the ADAM reflectometer [42].

4. Resonant magnetic X-ray scattering

The X-ray absorption cross-sections for right and left circularly polarized light at the L_2 and L_3 absorption edges of magnetic transition metals are different, the difference being the magnetic signal from the sample referred to as the X-ray magnetic circular dichroism (XMCD), as schematically depicted in Fig. 6. The element and magnetic sensitivity can also be used for scattering purposes, which is then referred to as the X-ray resonant magnetic scattering (XRMS).

Phenomenologically the X-ray scattering amplitude of an atom can be written in the form

$$f(Q,\omega) = f^0(Q) + f'(\omega) + if''(\omega) \tag{1}$$

where $f^0(Q)$ is the atomic form factor, i.e. the Fourier transform of the charge distribution, f', f'' are the real and
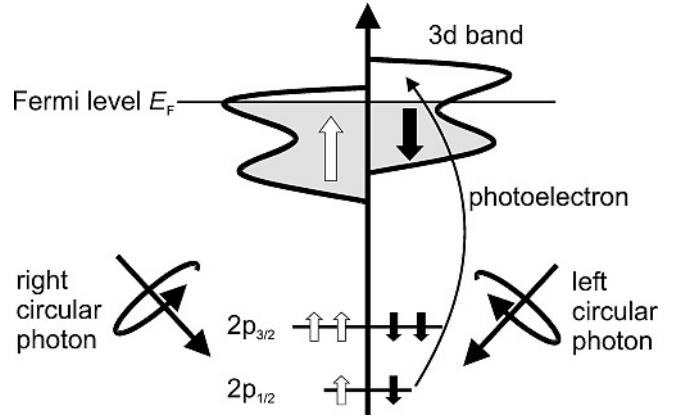

Fig. 6. Picture of the spin-dependent absorption process.

imaginary parts of the dispersion corrections, $Q = 4\pi/\lambda \sin(\theta)$ is the magnitude of the scattering vector, and ω is the X-ray frequency. f', f'' are energy dependent and take their extreme values at the absorption edges. Since the dispersion corrections are usually dominated by electrons in the K or L shell, where the electrons are spatially confined, their Q dependence can be neglected. The Thomson term f^0, on the other hand, depends on the scattering vector. However, at the 2p edges of 3d metals the X-ray wavelength is large compared to the atomic radius, which leads to the approximation $f^0(Q = 0) \cong Z$, where Z is the atomic charge number. If only dipole transitions are considered, the total elastic X-ray scattering amplitude can be written as [43–45]:

$$f = \underbrace{(\epsilon_f^* \cdot \epsilon_i)(-r_eZ + F^{(0)})}_{f_1} + \underbrace{i(\epsilon_f^* \times \epsilon_i) \cdot mF^{(1)}}_{f_2} + \underbrace{(\epsilon_f^* \cdot m)(\epsilon_i \cdot m)F^{(2)}}_{f_3} \tag{2}$$

where with $\epsilon_{i,f}$ are the unit polarization vectors of the incident and scattered waves, respectively. The $F^{(i)}$ functions are defined as follows:

$$F^{(0)} = \frac{3\lambda}{8\pi}\left[F_{-1}^1 + F_1^1\right] \tag{3}$$

$$F^{(1)} = \frac{3\lambda}{8\pi}\left[F_{-1}^1 - F_1^1\right] \tag{4}$$

$$F^{(2)} = \frac{3\lambda}{8\pi}\left[2F_0^1 - F_{-1}^1 - F_1^1\right] \tag{5}$$

The unit vector m points along the direction of the local magnetic moment, which defines the quantization axis of the system. The functions $F^{0,1,2}$ are strongly energy dependent resonant strengths for the dipole transitions. The first term in Eq. (2) refers to non-resonant and resonant charge scattering. The second term is first order in the magnetization and yields a circular dichroic signal, whereas the third term is second order in the magnetization causing linear dichroism. The XRMS experiments reported here used the L-MOKE geometry, where the magnetization lies along the sample surface within the scattering plane. To probe this magnetization, circular polarized light is needed. The polarization vectors can be written as a linear combination of ϵ_π and ϵ_σ

$$\epsilon_\pm = \mp\frac{1}{\sqrt{2}}(\epsilon_\sigma \pm i\epsilon_\pi) \tag{6}$$

where ϵ_π and ϵ_σ refer to the polarization vectors parallel and perpendicular to the scattering plane, respectively, and the positive sign indicates right circular polarization. The refractive index is related to the scattering amplitude through

$$1 - n(\omega) = \frac{r_e \lambda^2}{2\pi} \sum_i \rho_i f_i(\omega, Q = 0) \tag{7}$$

where ρ_i is the number density of species i in the sample and $f_i(\omega, Q = 0)$ is the corresponding scattering amplitude in the forward direction $k_i = k_f$ [46]. It can be shown that the classical optical approach and the quantum-mechanical description are equivalent with respect to the dipolar transitions [47]. However, for the simulation of specular reflectivity from ferromagnetic multilayer systems an algorithm based on magneto-optics is more convenient, since it allows for the application of a standard dynamic approach. The required refractive index of a material can be completely inferred by an absorption experiment. The refractive index is commonly split into real and imaginary parts according to

$$n_\pm = 1 - \delta_\pm + i\beta_\pm = 1 - (\delta \pm \Delta\delta/2) + i(\beta \pm \Delta\beta/2) \tag{8}$$

where δ and β are the dispersive and absorptive contributions, respectively, and $\Delta\delta$ and $\Delta\beta$ are the corresponding magnetic contributions to the refractive index. According to the optical theorem, the imaginary part β of the complex refractive index is directly proportional to the absorption coefficient μ,

$$\beta_\pm = \mu_\pm/(2k) \tag{9}$$

where k is the photon wavevector and the index refers to positive ($+$) or negative ($-$) circular polarization. If the energy dependence of β is known, the modified Kramers–Kronig relations

$$\delta_+(E) + \delta_-(E) = -\frac{2}{\pi}\mathcal{P}\int_0^\infty E'\frac{\beta_+(E') + \beta_-(E')}{E'^2 - E^2}\,dE' \tag{10}$$

$$\delta_+(E) - \delta_-(E) = -\frac{2E}{\pi}\mathcal{P}\int_0^\infty \frac{\beta_+(E') - \beta_-(E')}{E'^2 - E^2}\,dE' \tag{11}$$

can yield the dispersive contribution δ to the refractive index. $\mathcal{P}$ denotes the principal value of the integral [48].

X-ray resonant magnetic scattering allows for the determination of element-specific chemical and magnetic depth profiles of layered structures [49–51]. These profiles can be obtained by a quantitative analysis of specular reflectivity measurements, usually performed by numerical simulation. The calculation of the reflectivity needs a dynamic approach, since total and multiple reflection effects cannot be neglected. Lee et al. have given a theoretical formulation of X-ray resonant magnetic scattering [52, 53] from rough surfaces and interfaces within the distorted-wave Born approximation. A matrix based formalism for magneto-optics with arbitrary magnetization direction has been developed by Zak et al. [54–56]. It offers the possibility to calculate the specular reflectivity without any restrictions to the geometry, i.e. the magnetization direction, angle of incidence and polarization.

For the present XRMS measurements circularly polarized light in the energy range of 600–900 eV was used. A magnetic field was applied in the scattering plane along the sample surface either parallel or antiparallel to the photon helicity, which corresponds to the longitudinal magneto-optical Kerr effect (L-MOKE) geometry. The maximum field was ± 1.1 kOe, high enough to fully saturate the ferromagnetic Co$_2$MnGe layers. The magnetic contribution to the scattered intensity was measured by reversing the magnetic field while keeping the photon helicity fixed. For more details we refer readers to Refs. [57, 58] and references therein.

5. Polarized neutron reflectivity

As the wavevector transfer is small in neutron reflectivity (NR) experiments, the layer average nuclear and magnetic density profile normal to the surface is probed. If the neutron polarization, i.e. the neutron magnetic moment is fixed and the polarization state of the scattered neutrons is analyzed before the detector, NR is called polarized neutron reflectivity (PNR). In our experiments four reflectivity curves are measured, denoted as $R^{++}, R^{--}, R^{+-}, R^{-+}$. Here the first index '+' or '−' refers to the incident neutron spin state, and the second index to the neutron spin state after reflection from the sample. The reflectivities R^{++} and R^{--} are those without a change in the spin state and are called non-spin-flip (NSF) channels, whereas R^{+-} and R^{-+} are spin-flip (SF) channels. The scattering geometry for PNR studies is schematically depicted in Fig. 7. The y-axis is the quantization axis for the neutron magnetic moment μ_N, which is interacting with the in-plane magnetic induction B in the sample. For specular reflectivity $\alpha_i = \alpha_f$ holds and the scattering vector Q_z is parallel to the z-axis and perpendicular to the surface.

In the dynamic theory, the scattering of polarized neutrons can be calculated in an exact way, starting from basic equations. By fitting a model reflectivity to the measured polarized neutron reflectivities, the depth-dependent magnetization profile can be derived in addition to structural information like film thickness and interfacial roughness.

Considering the two possible eigen-states of the neutron, the particle behavior is formally described by a two-component vector of states, i.e. $\Psi(z) = (\Psi_+(z), \Psi_-(z))$, $\Psi_+(z)$ for neutrons polarized parallel to the y-direction, and
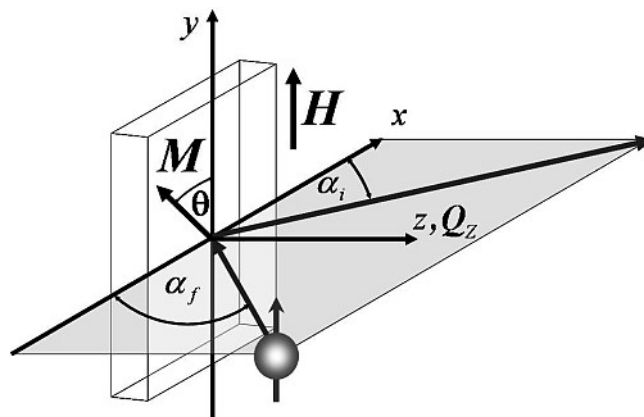

Fig. 7. Scattering geometry for PNR studies. The y-axis is the direction of the applied field and therefore also the quantizitation axis for the neutrons and the non-spin-flip axis, while the x-direction is the spin-flip axis. For specular reflectivity studies the scattering vector Q is parallel to the z-axis.

A. Bergmann et al. Heusler films and multilayers: X-ray resonant magnetic scattering

$\Psi_-(z)$ for neutrons polarized antiparallel to the y-direction. The specular scattering of polarized neutrons is then described by a pair of coupled, second order differential equations:

$$\frac{\partial^2}{\partial z^2}\Psi_+(z) + \left(\frac{Q^2}{4} - \frac{2m}{\hbar^2}V_{++}(z)\right)\Psi_+(z)$$

$$- \frac{2m}{\hbar^2}V_{+-}(z)\Psi_-(z) = 0 \qquad (12)$$

$$\frac{\partial^2}{\partial z^2}\Psi_-(z) + \left(\frac{Q^2}{4} - \frac{2m}{\hbar^2}V_{--}(z)\right)\Psi_-(z)$$

$$- \frac{2m}{\hbar^2}V_{-+}(z)\Psi_+(z) = 0 \qquad (13)$$

where the total scattering potential seen by the neutrons can be written as an operator V:

$$\begin{pmatrix} V_{++} & V_{+-} \\ V_{-+} & V_{--} \end{pmatrix} = \frac{2\pi\hbar^2}{m}N\left[\begin{pmatrix} b_n & 0 \\ 0 & b_n \end{pmatrix} + \begin{pmatrix} b_y & b_x \\ b_x & -b_y \end{pmatrix}\right] \qquad (14)$$

Here m is the neutron mass, $\hbar$ is the Planck constant, b_n is the coherent neutron scattering length, and the non-diagonal elements $V_{\pm\mp} \propto b_x = b_m \sin\theta$ are proportional to the component of magnetic induction perpendicular to the polarization axis. The diagonal elements $V_{\pm\pm} \propto (b_n \pm b_y)$ depend on $b_y = b_m \cos\theta$, i.e. on the inductance component parallel to the y-axis, where b_m can be considered as the magnetic scattering length.

Some conclusions can directly be drawn without solving the Schrödinger equation. When the off-diagonal elements of the scattering potential $V_{i,j}$ with $i \neq j$ are zero, Eqs. (12) and (13) are decoupled and only NSF scattering occurs. In this case the vector of the magnetic induction of the sample B has to be oriented along the y-axis. Alternatively, if the magnetization is aligned parallel to the x-axis, $V_{i,j}$ with $i = j$ are zero and the V_{+-}, V_{-+} potentials flip the neutron spin from up to down and vice versa. Thus quantitative analysis of all four scattering channels in a PNR experiment allows for the determination of the magnitude and orientation of the magnetic induction in the sample.

For the analysis of the measured reflectivities some important points should be noted here. The diagonal elements of the scattering potential V_{++} and V_{--} contain nuclear as well as magnetic contributions, whereas V_{+-} and V_{-+} are solely of magnetic origin. As the 'up' and 'down' neutrons experience different scattering potentials when interacting with a ferromagnetic sample, the critical vector for the total reflection Q_c has to be modified. For the case of NSF scattering Q_c is given by [59]

$$Q_c^\pm = \sqrt{16\pi\rho_a(b_n \pm b_m)}\,\hat{z} \qquad (15)$$

Here $\pm$ refers to the up and down spin polarization, and $\hat{z}$ is a unit vector pointing in the direction of the scattering vector normal to the surface.

For an angle Θ of the magnetization vector with respect to the y-axis, the difference

$$R^{++} - R^{--} = 2b_m \cos\theta \propto 2B_y \qquad (16)$$

is proportional to the y-component of the magnetization vector, whereas the spin-flip reflectivities are degenerate, and

$$R^{+-} + R^{-+} = 2b_m \sin^2\theta \propto B_x^2 \qquad (17)$$

is proportional to the square of the x-component of the magnetic induction.

The solution of Eqs. (12) and (13) will not be given here, but several algorithm to simulate PNR data have been provided in the literature [60–62], among them the supermatrix (SM) method and the matrix-recursion (MR) formalism [63–67]. These are based on a generalized Parratt formalism. A potential well structure composed of slabs of constant potential is assumed. Then all transmitted and reflected amplitudes are calculated via recursion. Interface roughness can be realized numerically by a slicing method [68], where the interface region is divided into different layers with sharp boundaries and constant potentials.

6 Scattering results of Heusler alloy multilayers

Using specular and off-specular hard X-ray reflectivity we have found that in Co_2MnGe/Au multilayers at the interfaces correlated roughness dominates and interdiffusion is negligible, whereas in Co_2MnGe/V multilayers the roughness is uncorrelated and dominated by interdiffusion. In Co_2MnGe/AlO_x multilayers, in contrast, the interfaces are very sharp, roughness and interdiffusion is negligible. A typical hard X-ray reflectivity scan from a $[Co_2MnGe$ (3 nm)/Au (3 nm)$]_{\times 50}$ multilayer is shown in Fig. 8. Here the subscript refers to the number of double layers and the layer thicknesses are nominal thicknesses. A theoretical fit to the data by the Parratt formalism (solid line) yields 2.29 (0.4 nm) nm and 2.93 nm (0.3 nm) for the Au and Heusler layer thicknesses (mean square interface roughness parameters), respectively.

With XRMS methods we have again recorded the reflectivity curves, but now with the incident circularly polarized X-ray beam tuned to the corresponding L_3 absorption edges of Co and Mn. The results are shown in Fig. 9. Included in this figure is, for comparison, the hard X-ray scan of the same multilayer. In the next step the scattering angles are
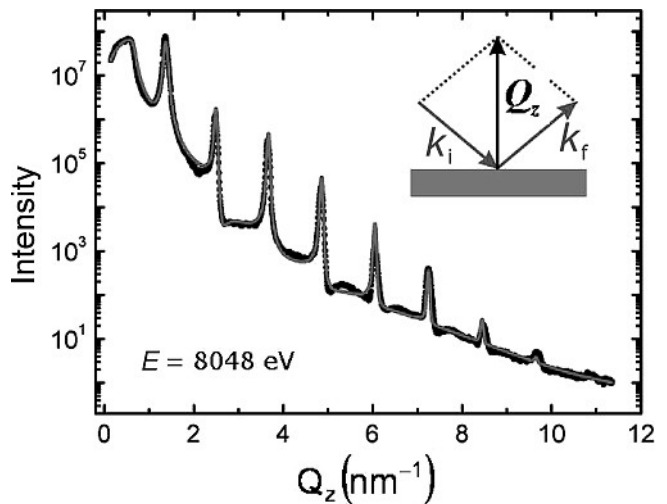

Fig. 8. Hard X-ray reflectivity from $[Co_2MnGe\ 2.3\ nm/Au\ 3\ nm]_{\times 50}$ multilayer. The solid line is a fit to the data points.

A. Bergmann et al. Heusler films and multilayers: X-ray resonant magnetic scattering

frozen to one of the multilayer Bragg peaks and the incident photon energy is scanned across the region of the L_2 and L_3 absorption edges. These energy scans reveal the element-specific magnetic moment density profiles within the Co_2MnGe layers [47, 57]. In Fig. 10 we show for the Co_2MnGe/Au multilayers the charge intensity $(I^+ + I^-)/2$ and the magnetically sensitive asymmetry $(I^+ - I^-)/(I^+ + I^-)$ for the first three Bragg peaks at the Co $L_{2,3}$ absorption edges. These spectra are very rich in structure due to convolution of charge and magnetic intensity and therefore not easy to analyze. However, from the sign dependence of the asymmetry some straightforward conclusions can be drawn about the non-ferromagnetic layer thickness, as shown by model calculations discussed in [57]. According to the asymmetry at the photon energy of 775 eV, which is (+.−.+) for the first, second, and third order Bragg peak, one can conclude by comparison with model calculations that the non-ferromagnetic interlayer must have a thickness
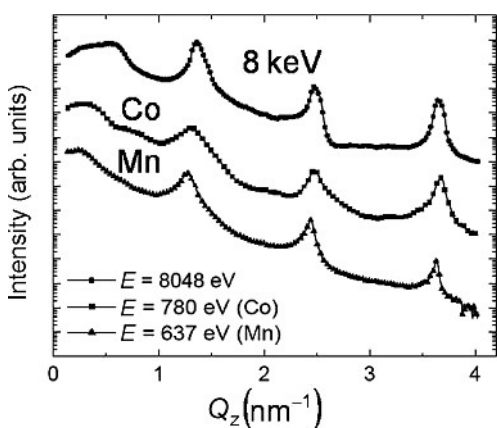
of about 1 nm. For a more refined estimate the energy-dependent intensities and asymmetries need to be modeled within a magneto-optical matrix formalism, as done for Co_2MnGe/Au in [57].

We find for all three types of Heusler multilayers that the magnetic moment density profiles determined for Co and Mn are definitely different. Moreover, they are narrower than the chemical density profiles, indicative of reduced moments at the interfaces and asymmetric profiles with respect to the growth direction. For Co_2MnGe/Au multilayers at room temperature a non-ferromagnetic interface layer exists with a thickness of about 0.6 nm at the bottom and 0.45 nm at the top of the Co_2MnGe layers; for Co_2MnGe/V multilayers at the bottom and the top the corresponding thicknesses are 0.5 nm and 0.35 nm, respectively. In Co_2MnGe/AlO_x multilayers the respective thicknesses are 1 nm and 0.5 nm. This enlarged thickness is plausible, since on an amorphous AlO_x layer it is most difficult to grow an ordered $L2_1$ structure with full magnetic moment. Therefore, the layer averaged magnetic moment in Co_2MnGe/AlO_x multilayers has the lowest value of about $2\mu_B$/f.u., compared to 2.25 μ_B in Co_2MnGe/V [69], and 2.35 μ_B in Co_2MnGe/Au [57].

We have also studied the interface quality and magnetization profile of Co_2MnGe/V and Co_2MnGe/AlO_x multilayers via PNR. In Fig. 11 intensity maps are shown as a function of incident and exit glancing angles α_i and α_f, respectively. The specular reflectivity runs along the diagonal $\alpha_i = \alpha_f$. The left panel shows the intensity map for a $[Co_2MnGe \ (3 \ nm)/V \ (3 \ nm)]_{50}$ multilayer. In this map, taken with an unpolarized incident neutron beam at zero field, the first order Bragg peak occurs at angles $\alpha_i = \alpha_f = 2.5°$. In addition, a half order antiferromagnetic (AF) Bragg peak at angles $\alpha_i = \alpha_f = 1.25°$ occurs at temperatures below 30 K. The antiferromagnetic coupling observed here is not due to oscillatory interlayer exchange coupling. It is rather due to a weak Néel-type coupling promoted by stray fields
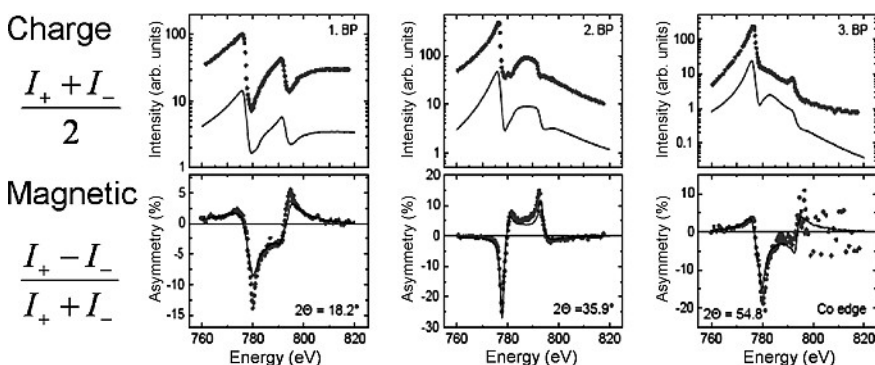

Fig. 9. Soft X-ray reflectivity from the same $[Co_2MnGe \ (3 \ nm)/Au \ (3 \ nm)]_{\times 50s}$ multilayer as shown in Fig. 8, but with X-ray energies fixed to the Co and Mn L_3 edges, respectively. The top plot is a reproduction of the hard X-ray scan shown in Fig. 8.

Fig. 10. Charge scattering and asymmetry for the first three Bragg peaks of the Co_2MnGe/Au measured close to the L_2 and L_3 resonances. 1. BP, 2. BP, and 3. BP refer to the first, second and third Bragg peak, as shown in Fig. 9. The dots represent measured data, the lines are model calculations. The theoretical charge intensity curves in the top panels are shifted down for clarity.
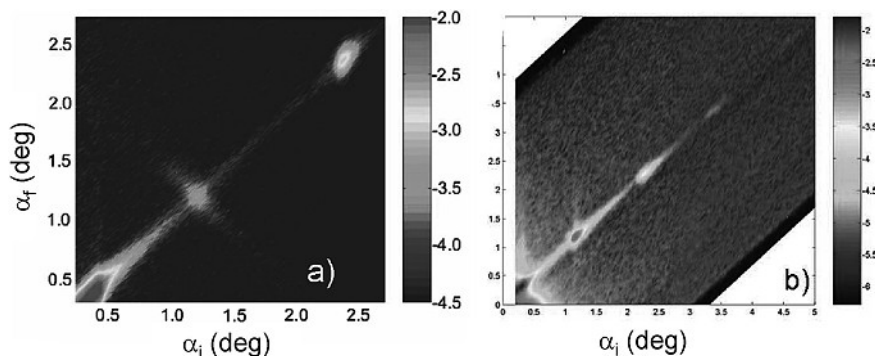

Fig. 11. Neutron reflectivity maps of Heusler alloy multilayers. (a) Reflectivity map of $[Co_2MnGe \ (3 \ nm)/V \ (3 \ nm)]_{50}$ multilayer; (b) Reflectivity map of a $[Co_2MnGe \ (3 \ nm)/AlO_x \ (9 \ nm)]_{50}$ multilayer.

Review

A. Bergmann et al. Heusler films and multilayers: X-ray resonant magnetic scattering

from the magnetic domains in the multilayer. The AF peak exhibits a pronounced streak perpendicular to the specular reflectivity ridge into the off-specular regime. This streak indicates highly correlated AF-coupled magnetic domains, which have a lateral size of about 3 μm, as determined by simulation of the off-specular diffuse intensity. In contrast, $[Co_2MnGe$ (3 nm)/AlO$_x$ (9 nm)]$_{50}$ multilayers only show a random distribution of magnetic clusters at high temperatures, which can be aligned below the blocking temperature of about 100 K in a high magnetic field. In Fig. 11b the corresponding intensity map is shown, using an incident (+) polarized beam without polarization analysis of the exit beam. The map was recorded at 10 K in a field of 1.3 kOe. Due to the much larger period of this multilayer and the increased scale, four orders of Bragg peaks can be recognized, which are due to the chemical and magnetic periodicity. There is no AF half order peak nor off-specular intensity, indicating that neither correlated structural nor correlated magnetic roughness is of any significance. We have also probed the diffuse scattering at low temperatures in remanence. The lack of appreciable diffuse scattering at 10 K indicates that the magnetic clusters are rather small and that they are uncorrelated.

In Fig. 12 we reproduce the specular R^{++} and R^{--} reflectivity data for a $[Co_2MnGe$ (3nm)/AlO$_x$ (9 nm)]$_{50}$ multilayer taken at 10 K and in a high field of 1.3 kOe. Under these conditions the sample is in saturation and ferromagnetic splitting between the R^{++} and R^{--} reflectivities can easily be recognized. Note that the R^{++} and R^{--} intensities cross beyond the third order Bragg peak. This is a clear sign for an asymmetric magnetization profile. In fact, we find the best fit to the data points assuming a magnetization profile of the Heusler layer with a 1.2 nm thick non-ferromagnetic layer at the bottom and a 0.5 nm non-ferromagnetic layer at the top. This asymmetry is similar to the other Heusler multilayers discussed above, but with a thicker non-ferromagnetic interface layer.

After saturation the $[Co_2MnGe$ (3 nm)/AlO$_x$ (9 nm)]$_{50}$ multilayer at low temperatures in a high field, we have removed the field and rotated the sample by 90°. In this case the remanent single domain state has a magnetization vector pointing along the spin-flip (SF) axis for polarized neutron scattering. The results are shown in Fig. 13. Parallel
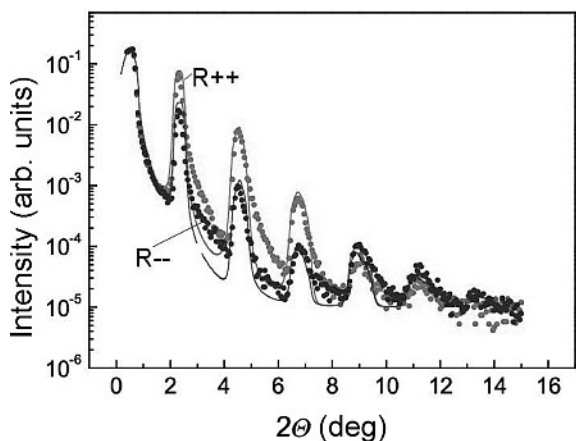

Fig. 12. Specular polarized neutron reflectivity of a $[Co_2MnGe$ (3 nm)/AlO$_x$ (9 nm)]$_{50}$ multilayer. The intensity crossing of the R^{++} and R^{--} at the fourth Bragg peak is an indication for an asymmetric density profile.
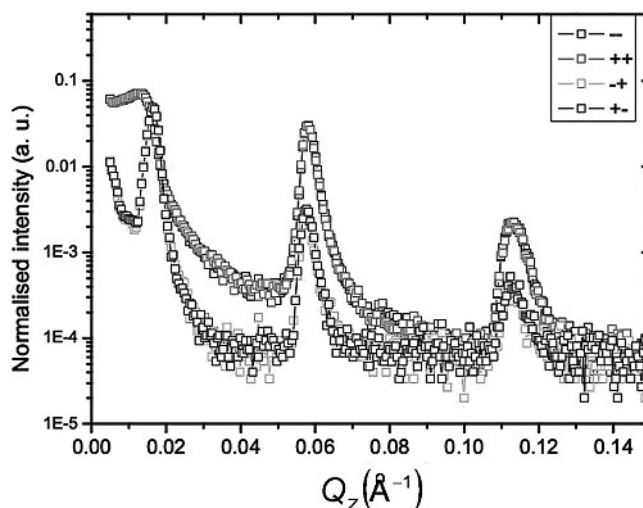

Fig. 13. Specular polarized neutron reflectivity of a $[Co_2MnGe$ (3 nm)/AlO$_x$ (9 nm)]$_{50}$ multilayer. The NSF reflectivity is solely due to the nuclear profile, while the SF reflectivity is entirely due to the magnetic profile. The separation of nuclear and magnetic scattering is achieved by first saturating the sample parallel to the y-axis and then rotating the sample in remanence, such that the magnetization vector isoriented parallel to the x-axis (SF-axis).

to the NSF direction, the ferromagnetic splitting between the R^{++} and R^{--} specular reflectivities vanishes, whereas strong SF scattering occurs, which is of pure magnetic origin. With this technique, the nuclear density profile (NSF) and the magnetic density profile (SF) can be separated and directly be compared. The Bragg peaks are shifted slightly against each other because of refractive effects in the NSF reflectivities. The shapes of the Bragg peaks are slightly different for NSF and SF scattering, indicative of different nuclear and magnetic density profiles in this multilayer.

7. Discussion and conclusions

The combination of hard X-ray scattering, soft X-ray resonant magnetic scattering, and polarized neutron reflectivity provides us with a wealth of detailed information on the structural properties (layer thickness, interface roughness, interdiffusion) and the magnetic properties (element specific magnetization profiles, magnetic domain state, and interlayer antiferromagnetic coupling). From hard X-ray scattering we find the layer thicknesses and the interfacial roughnesses. Resonant magnetic soft X-ray scattering provides the layer and elemental resolved profiles of the magnetic moments normal to the layers, which for the analysis of the Heusler alloys is essential to distinguish between the Co and Mn magnetization profiles. With polarized neutron reflectivity the average layer magnetization vector is probed and off-specular magnetic scattering yields information on the domain size distribution at remanence. Furthermore, any correlation normal to the layers can easily be recognized, such as the antiferromagnetic coupling in $[Co_2MnGe$ (3 nm)/V (3 nm)]$_{50}$ multilayers at low temperatures. Another important advantage of polarized neutron reflectivity is the fact that in the spin-flip channel the magnetic scattering can be separated from the nuclear scattering. A similar separation of charge and magnetic scattering is not possible in the case of resonant magnetic X-ray scattering.

A. Bergmann et al. Heusler films and multilayers: X-ray resonant magnetic scattering
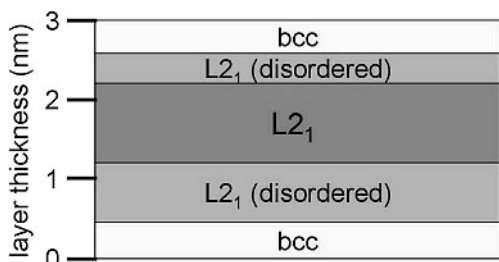
Fig. 14. Schematic profile of the interface region for Heusler/spacer multilayers.

We find for all Heusler multilayers a reduced magnetization at the interfaces, not only at the lower interface where the growth starts, but also at the top interface after covering with the spacer layer. In all cases, this interfacial layer with reduced magnetization is thicker at the bottom than at the top. For the $[Co_2MnGe/AlO_x]_{50}$ Heusler multilayer this effect is most pronounced. The interfacial profile at the top and bottom interfaces is shown schematically in Fig. 14. The non-magnetic layer close to the interface is referred to as bcc, as the random alloy has bcc structure and no magnetic moment. The intermediate layer is referred to as disordered $L2_1$, since the magnetic moments are reduced due to antisites. The exact nature of the antisites could not be analyzed by the methods employed here. The center Heusler layer is labelled as $L2_1$, as this layer exhibits the highest magnetic moment, close to the expected moment for the bulk ordered phase.

In the past magnetic tunnel junctions have been produced with one Heusler layer only where the top electrode is a ferromagnetic transition metal, for instance $Co_2MnGe/AlO_x/Co$ [70, 71]. In this case the bottom Heusler layer can be grown under optimized conditions on a single crystalline substrate, while the top layer shows ferromagnetism irrespective of the crystal quality. However, in a tunnel junction with two Heusler layers such as $Co_2MnGe/AlO_x/Co_2MnGe$ the top Heusler layer has to be grown on the amorphous AlO_x barrier layer. This will immediately cause growth problems which severely hamper the magnetization and spin polarization at the AlO_x/Co_2MnGe interface. The way out of the problem is the use of single crystalline tunnel barriers, such as MgO. Indeed with the use of MgO tunnel barriers, very high values for the tunneling magneto-resistance have recently been observed [72].

References

[1] G.A. Prinz: Science 282 (1998) 1660.
[2] D. Awschalom, J. Kikkawa: Physics Today 52 (1999) 33.
[3] J.F. Gregg, I. Petey, E. Jougelet, C. Dennis: J. Phys. D: Appl. Phys. 35 (2002) R121.
[4] R. de Groot, P. van Engen: Phys. Rev. Lett. 50 (1983) 2024.
[5] I. Galanakis, P.H. Dederichs, N. Papanikolaou: Phys. Rev. B 66 (2002) 174429.
[6] S. Picozzi, A. Continenza, A.J. Freeman: Phys. Rev. B 69 (2004) 094423.
[7] I. Galanakis, P.H. Dederichs, N. Papnikolaou: Phys. Rev. B 66 (2002) 134428.
[8] M.P. Raphael, B. Ravel, Q. Huang, M.A. Willard, S.F. Cheng, B.N. Das, R.M. Stroud, K.M. Bussmann, J.H. Claassen, V.G. Harris: Phys. Rev. B 66 (2002) 104429.
[9] C. Felser, B. Heitkamp, F. Kronast, D. Schmitz, S. Cramm, H.A. Dürr, H-J. Elmers, G.H. Fecher, S. Wurmehl, T. Block, D. Valdaitsev, S.A. Nepijko, A. Gloskovskii, G. Jakob, G. Schoenhense, W. Eberhardt: J. Phys.: Condens. Matter 15 (2003) 7019.
[10] C.T. Tanaka, J. Nowak, J.S. Moodera: J. Appl. Phys. 86 (1999) 6239.
[11] Y. Sakuraba, J. Nakata, M. Oogane, H. Kubota, Y. Ando, A. Sakuma, T. Miyazaki: Japan. J. Appl. Phys. 44 (2005) L1100.
[12] M. Oogane, Y. Sakuraba, J. Nakata, Y. Ando, A. Sakuma, T. Miyazaki: J. Phys. D: Appl. Phys. 39 (2006) 834.
[13] S. Ishida, T. Masaki, S. Fujii, S. Asano: Physica B 245 (1998) 1.
[14] I. Galanakis: J. Phys.: Condens. Matter 14 (2002) 6329.
[15] F. Heusler: Verh. Dtsch. Phys. Ges. 5 (1903) 219.
[16] P.J. Ziebeck, K.R.A. Webster: Landolt-Bornstein New Series III/19c (1986).
[17] S. Ishida, S. Fujii, S. Kashiwagi: Journal of the Physical Society of Japan 64 (1995) 2152.
[18] S. Picozzi, A. Continenza, A.J. Freeman: Phys. Rev. B 66 (2002) 094421.
[19] Y. Miura, K. Nagao, M. Shirai: Phys. Rev. B 69 (144413) 2004.
[20] K.R.A. Ziebeck, P.J. Webster: J. Phys. F 5 (1975) 1756.
[21] P.J. Webster, R.S. Tebbel.: J. Appl. Phys. 39 (1968) 471.
[22] P.J. Webster: J. Phys. Chem. Sol. 32 (1971) 1221.
[23] K.H.J. Buschow, P.G. van Engen: J. Magn. Mag. Mat. 25 (1983) 90.
[24] J. Kübler, A.R. Williams, C.B. Sommers: Phys. Rev. B 28 (1983) 1745.
[25] I. Galanakis, P.H. Dederichs: Half-metallicity and Slater-Pauling Behavior in the Ferro-magnetic Heusler Alloys. In: P.H. Dederichs, J. Galanakis, editors, Half-metallic Alloys – Fundamentals and Applications, Lecture Notes in Physics. Springer, 2005.
[26] S. Fujii, S. Sugimura, S. Ispida, S. Asano: J. Phys.: Cond. Matter 2 (1990) 8583.
[27] S. Ishida, S. Kashiwagi, S. Fujii, S. Asano: Physica B 210 (1995) 140.
[28] P.J. Brown, K.U. Neumann, P.J. Webster, K.R.A. Ziebeck: J. Phys.: Cond. Matter 12 (2000) 1827.
[29] L. Ritchie, G. Xiao, Y. Ji, T.Y. Chen, M. Zhang, C.L. Chien, M. Zhang, J. Chen, Z. Liu, G. Wu, X.X. Zhang: Phys. Rev. B 68 (2003) 104430.
[30] D. Ristoiu, J.P. Nozieres, C.N. Borca, T. Komesu, H.-K. Jeong, P.A. Dowben: Europhys. Lett. 49 (2000) 624.
[31] W. Zhu, B. Sinkovic, E. Vescovo, C. Tanaka, J.S. Moodera: Phys. Rev. B 64 (2001) 060403(R).
[32] B. Ravel, J.O. Cross, M.P. Raphael, V.G. Harris, R. Ramesh, V. Saraf: Appl. Phys. Lett. 81 (2002) 2812.
[33] X.Y. Dong, C. Adelmann, J.Q. Xie, C.J. Palmstrøm, X. Lou, J. Strand, P.A. Crowell, J.-P. Barnes, A.K. Petford-Long: Appl. Phys. Lett. 86 (2005) 102107.
[34] T. Ambrose, J.J. Krebs, G.A. Prinz: J. Appl. Phys. 87 (2000) 5463.
[35] M. Yamamoto, T. Ishikawa, K. Matsuda, T. Uemura, M. Arita: J. Phys. D: Appl. Phys. 39 (2006) 824.
[36] G.A. de Wijs, R.A. de Groot: Phys. Rev. B 64 (2001) 020402.
[37] A. Debernadi, M. Peressi, A. Baldereschi: Mat. Sci. Eng. C 23 (2003) 743.
[38] I. Galanakis, P. Mavropoulos, P.H. Dederichs: J. Phys. D: Appl. Phys. 39 (2006) 765.
[39] S. Picozzi, A. Continenza, A.J. Freeman: J. Appl. Phys. 94 (2003) 4723.
[40] U. Geiersbach, A. Bergmann, K. Westerholt: Thin Solid Films 425 (2003) 226.
[41] J. Grabis, A. Nefedov, H. Zabel: Rev. Sci. Instr. 74 (2003) 4048.
[42] A. Scheyer, R. Siebrecht, U. English, U. Pietsch, H. Zabel: Physica B 267–268 (1999) 355.
[43] J.P. Hannon, G.T. Trammell, M. Blume, D. Gibbs: Phys. Rev. Lett. 61 (1988) 1245.
[44] B.T. Thole, P. Carra, F. Sette, G. van der Laan: Phys Rev Lett. 68 (1992) 1943.
[45] P. Carra, B.T. Thole: Rev. Mod. Phys. 66 (1994) 1509.
[46] R.W. James: The Optical Principles of the Diffraction of X-Rays. Oxbow Press(1982).
[47] J.B. Kortright, S.-K. Kim: Phys. Rev. B 62 (2000) 12216.
[48] D. McMorrow, J. Als-Nielsen: Modern X-Ray Physics. John Wiley & Son, Ltd. (2001).
[49] J. M. Tonnerre, L. Seve, D. Raoux, G. Soullie, B. Rodmacq, P. Wolfers: Phys. Rev. Lett. 75 (1995) 740.
[50] N. Jaouen, J.M. Tonnerre, D. Raoux, E. Bontempi, L. Ortega, M. Muenzenberg, W. Felsch, A. Rogalev, H.A. Dürr, E. Dudzik,

R Review

A. Bergmann et al. Heusler films and multilayers: X-ray resonant magnetic scattering

G. van der Laan, H. Maruyama, M. Suzuki: Phys. Rev. B 66 (2002) 134420.

[51] J. Geissler, E. Goering, M. Justen, F. Weigand, G. Schutz, J. Langer, D. Schmitz, H. Maletta, R. Mattheis: Phys. Rev. B 65 (2002) 020405(R).

[52] D.R. Lee, S.K. Sinha, D. Haskel, Y. Choi, J.C. Lang, S.A. Stepanov, G. Srajer: Phys. Rev. B 68 (2003) 224409.

[53] D.R. Lee, S.K. Sinha, C.S. Nelson, J.C. Lang, C.T. Venkataraman, G. Srajer, R.M. Osgood III: Phys. Rev. B 68 (2003) 224410.

[54] J. Zak, E.R. Moog, C. Liu, S.D. Bader: J. Magn. Magn. Mat. 89 (1990) 107.

[55] J. Zak, E.R. Moog, C. Liu, S.D. Bader: Phys. Rev. B 43 (1991) 6423.

[56] J. Zak, E.R. Moog, C. Liu, S.D. Bader: Phys. Rev. B 46 (1992) 5883(E).

[57] J. Grabis, A. Bergmann, A. Nefedov, K. Westerholt, H. Zabel: Phys. Rev. B 72 (2005) 024437.

[58] A. Bergmann, J. Grabis, A. Nefedov, K. Westerholt, H. Zabel: J. Phys. D: Appl. Phys. 39 (2006) 842.

[59] H. Zabel, K. Theis-Bröhl: J. Phys: Condens. Matter, 15 (2003) S505.

[60] G.P. Felcher, R.O. Hilleke, R.K. Crawford, J. Haumann, R. Kleb, G. Ostrowski: Rev. Sci. Instrum. 58 (1987) 609.

[61] C.F. Majkrzak: Physica B 156, 157 (1989) 619.

[62] C.F. Majkrzak: Physica B 173 (1991) 75.

[63] F. Radu, V.K. Ignatovich: Physica B 268 (1999) 175.

[64] A. Rühm, B.P. Toperverg, H. Dosch: Phys. Rev. B 60 (1999) 16073.

[65] B. P. Toperverg: Physica B 297 (2001) 160.

[66] B.P. Toperverg, A. Rühm, W. Donner, H. Dosch: Physica B 267–268 (1999) 198.

[67] B.P. Toperverg, in: Th. Brückel, W. Schweika (Eds.), Polarized Neutron Reflection and off-specular Scattering. Polarized Neutron Scattering, Matter and Materials, Vol. 12. (2002) Schriften des Forschungszentrums Julich.

[68] S.A. Stepanov, R. Köhler: J. Appl. Phys. 76 (1994) 7809.

[69] A. Bergmann, J. Grabis, B.P. Toperverg, V. Leiner, M. Wolff, H. Zabel, K. Westerholt: Phys. Rev. B 72 (2005) 214403.

[70] J. Schmalhorst, S. Kmmerer, M. Sacher, G. Reiss, A. Hutten, A. Scholl: Phys. Rev. B 70 (2004) 024426.

[71] E. Verduijn, K. Westerholt: J. App. Phys. 99 (2006) 084502.

[72] Y. Sakuraba, M. Hattori, M. Oogane, Y. Ando, H. Kato, A. Sakuma, T. Miyazaki, H. Kubota: Appl. Phys. Lett. 88 (2006) 192508.

Correspondence address

Prof. H. Zabel
Fakultät für Physik und Astronomie
Ruhr-Universität Bochum
D-44780 Bochum
Germany
Tel.: +49 0 234 322 3649
Fax: +49 0 234 321 4173
E-mail: hartmut.zabel@rub.de

You will find the article and additional material by entering the document number MK101660 on our website at www.ijmr.de